

Large off diagonal exchange couplings and spin liquid states in C_3 symmetric iridates

Ravi Yadav,¹ Satoshi Nishimoto,^{1,2} Manuel Richter,^{1,3} Jeroen van den Brink,^{1,2} and Rajyavardhan Ray^{1,3,*}

¹*IFW Dresden, Helmholtzstr. 20, 01069 Dresden, Germany*

²*Department of Physics, TU Dresden, D-01062, Dresden, Germany*

³*Dresden Center for Computational Materials Science (DCMS), TU Dresden, 01062 Dresden, Germany*

(Dated: September 6, 2019)

Iridate oxides on a honeycomb lattice are considered promising candidates for realization of quantum spin liquid states. We investigate the magnetic couplings in a structural model for a honeycomb iridate K_2IrO_3 , with C_3 point group symmetry at the Ir sites, which is an end member of the recently synthesized iridate family $K_xIr_yO_2$. Using *ab-initio* quantum chemical methods, we elucidate the subtle relationship between the real space symmetry and magnetic anisotropy and show that the higher point group symmetry leads to high frustration with strong magnetic anisotropy driven by the unusually large off-diagonal exchange couplings (Γ 's) as opposed to other spin-liquid candidates considered so far. Consequently, large quantum fluctuations imply lack of magnetic ordering consistent with the experiments. Exact diagonalization calculations for the fully anisotropic K - J - Γ Hamiltonian reveal the importance of the off-diagonal anisotropic exchange couplings in stabilizing a spin liquid state and highlight an alternative route to stabilize spin liquid states for ferromagnetic K .

I. INTRODUCTION

The possibility to realize a spin liquid (SL) state in condensed matter systems is being intensively investigated from both theoretical and experimental standpoints [1–3]. SL states are characterized by large degeneracy in the ground state, suppression of long-range (magnetic) order, and cannot be described by the broken symmetries associated with conventional magnetic ground states [4]. In this regard, most promising candidates are the spin-orbit-driven Mott insulators on a honeycomb lattice [5], such as Na_2IrO_3 [6, 7], α - Li_2IrO_3 [8, 9], and α - $RuCl_3$ [10–12]. Due to d^5 configuration in the presence of octahedral crystal field environment and spin-orbit coupling (SOC), the low-energy electronic properties is typically described by an effective nearest-neighbor Kitaev-Heisenberg Hamiltonian (K - J Hamiltonian) acting in the $j_{\text{eff}} = 1/2$ subspace. Large ratio of Kitaev to Heisenberg couplings, $K/J \gg 1$, found in these materials imply strong magnetic anisotropy and proximity to a SL state. However, presence of extended range magnetic couplings and small but finite J renders a long-range magnetic order instead [13–16].

Most of the works in these honeycomb lattice iridates have, therefore, focused on studying the effects of external stimulus, such as magnetic field [12, 17], hydrostatic pressure [18–20], trigonal distortions [16], as well as chemical substitutions and doping [21, 22], in order to tune the magnetic couplings favorably for a SL state. Very recently, a new family of honeycomb lattice iridates, $K_xIr_yO_2$ has been synthesized and in a substantial range of concentrations, including the end member K_2IrO_3 , a structural model featuring a C_3 point

group (PG) symmetry at the Ir sites was proposed [23, 24]. The magnetic susceptibility measurements suggest that no long-range order or spin freezing develops down to 1.8K while the specific heat is finite at low temperatures, implying the possibility of a gapless quantum SL state.[24]

Here, we report the influence of C_3 point group symmetry at the transition metal ion site on the nearest neighbor (NN) magnetic interactions between Ir atoms. Starting with the proposed structural model for K_2IrO_3 , we discuss the evolution of the magnetic couplings with deviations from the high symmetry structure and implications for the stability of a SL state. The NN magnetic couplings are obtained using quantum chemistry electronic structure calculations, performed for a crystal structure with optimized atomic positions as obtained within density functional theory (DFT). We find unusually large off-diagonal exchange couplings: $\Gamma_{xy} \sim 5$ meV and $\Gamma_{yz} \sim -9$ meV (in the local Kitaev frame), approximately 10 times larger than in Na_2IrO_3 . At the same time, while the K and J exchange terms are smaller, K/J ratio is comparable to other honeycomb iridates, thus, motivating a K - J - Γ Hamiltonian as an appropriate model to capture the underlying physics in K_2IrO_3 . We identify the origin of such large Γ 's as constraints on the relative orientation of the O-O pairs within the IrO_6 octahedra due to C_3 PG symmetry at the Ir sites imposed by the large K ions. The large Γ -driven magnetic anisotropy implies strong magnetic frustration and is responsible for suppression of magnetic ordering, observed experimentally.

We note that there is an emerging consensus regarding the importance of Γ terms in understanding the magnetic interactions in honeycomb lattice Mott insulators. Therefore, models involving such terms are being investigated. For example, an anisotropic Γ as well as a K - Γ model on a honeycomb lattice supports a SL state [25, 26]. The Γ -terms are also found to be

* r.ray@ifw-dresden.de

important in explaining the recent neutron scattering and high-temperature magnetic susceptibility experiments in α - RuCl_3 [27, 28]. However, these works consider only one component of Γ per bond, as opposed to our findings for the C_3 -symmetric structure.

Our exact diagonalization (ED) calculations using the quantum chemical NN magnetic couplings for K_2IrO_3 reveal that the fate of a SL state in the fully anisotropic K - J - Γ Hamiltonian is determined by the relative signs of Γ_{ij} 's: a Γ -driven SL state is found to be stable for small values of $\Gamma_{ij} < 0$ and spread over a large region in the Γ_{xy} - Γ_{yz} plane. Moreover, the ferromagnetic–Kitaev–SL–stripy path of the K - J model [5] is also recovered at finite Γ_{ij} 's. Further inclusion of extended range Heisenberg couplings suggest competing magnetic orders in K_2IrO_3 which may have interesting implications for magnetism.

II. RESULTS AND DISCUSSIONS

A. Structural details

In the proposed structural model, $\text{K}_x\text{Ir}_y\text{O}_2$ ($1 \lesssim x/y < 2$) crystallizes in the high symmetry space group $P6_322$ (# 182) [23] as opposed to $C2/m$ for the related iridate Na_2IrO_3 [6]. For brevity, we focus on the stoichiometric end member K_2IrO_3 , corresponding to $x = 4/3$ and $y = 2/3$. Starting from the experimental values of the external parameters, the atomic positions were optimized using DFT utilizing the space group symmetries (see Methods and Supplemental Material).

The resulting structure features alternating layers of non-magnetic cations (K ions, in this case) and a two-dimensional/planar honeycomb network of IrO_6 octahedra. Within the planar honeycomb network, the transition metal (TM) ions span a regular honeycomb lattice and share O-O edges between them (see Fig. 1). Within each honeycomb plane, one K ion is also present at the center of the hexagons. As compared to Na_2IrO_3 , the TM-ligand distance $d_{\text{Ir-O}} = 2.07 \text{ \AA}$ is comparable, while the TM-TM distance $d_{\text{Ir-Ir}} = 3.05 \text{ \AA}$ and the TM-O-TM angle $\angle \text{Ir-O-Ir} = 95.06^\circ$ are much smaller (see the Supplemental Material). Further notable differences with the related iridate Na_2IrO_3 are (i) the larger inter-layer separation: the two Ir (or, K) layers are separated by approximately 6.8 \AA , as opposed to 5.6 \AA in Na_2IrO_3 ; (ii) Each IrO_6 octahedron has a C_3 symmetry about the ‘c’ axis centered at the Ir atoms. As a result, a highly symmetric real space structure is realized where the projection of O-O links at every Ir-Ir bonds on the honeycomb plane are at 120° relative to each other, shown in Fig. 1(b).

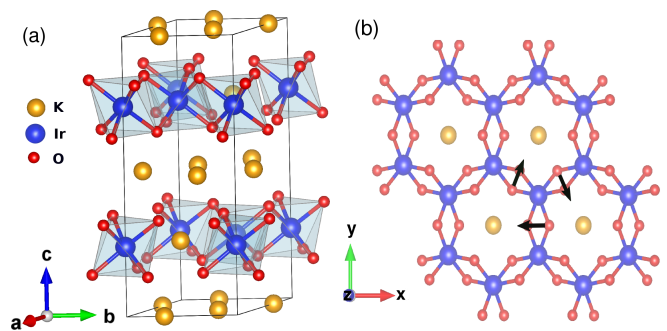


FIG. 1. Crystal structure of K_2IrO_3 : (a) shows the alternating layers formed of K ions, and hexagonal network formed by IrO_6 octahedra with K ions at the center of the hexagons. (b) Top view of the honeycomb plane spanned by the IrO_6 octahedra and K ions at center. Manifestation of the C_3 PG symmetry: the in-plane projections of the O-O links in each Ir_2O_2 plaquette are oriented 120° with respect to each other (shown by arrow from the O atoms above the Ir plane to O atoms below the Ir plane).

B. Electronic properties and magnetic couplings

The Ir- $5d$ levels in the presence of an octahedral ligand field split into e_g and t_{2g} levels, with the latter lying at significantly lower energy [29] (also see the Supplemental Material). The large crystal field splitting results in t_{2g}^5 configuration yielding effectively one hole per site. Strong spin-orbit coupling further splits the t_{2g} states into fully occupied $j_{\text{eff}} = 3/2$ and half-filled $j_{\text{eff}} = 1/2$ states [30–32]. Deviations from an ideal octahedral environment may lead to some admixture between these j_{eff} states.

The nearest-neighbor (NN) magnetic interactions were derived using quantum chemistry calculations performed on embedded clusters consisting of two edge-shared octahedra (Ir_2O_{10} units) plus their NN octahedral units and NN K ions (see Methods). At each Ir-Ir bond in K_2IrO_3 , this structural unit has an approximate C_{2h} point-group symmetry. Since the deviation from the C_{2h} symmetry is very small ($\lesssim 0.1\%$; see the Supplemental Material), an antisymmetric Dzyaloshinskii-Moriya (DM) term, which is not allowed in C_{2h} symmetry due to the presence of an inversion center, is expected to be negligible. Therefore, a generalized bilinear Hamiltonian between a pair of pseudospins $\tilde{\mathbf{S}}_i$ and $\tilde{\mathbf{S}}_j$ is obtained for the C_{2h} symmetry of the structural unit [15]:

$$\mathcal{H}_{ij}^{(\gamma)} = J \tilde{\mathbf{S}}_i \cdot \tilde{\mathbf{S}}_j + K \tilde{S}_i^\gamma \tilde{S}_j^\gamma + \sum_{\alpha \neq \beta} \Gamma_{\alpha\beta} (\tilde{S}_i^\alpha \tilde{S}_j^\beta + \tilde{S}_i^\beta \tilde{S}_j^\alpha), \quad (1)$$

where, J and K are the Heisenberg and Kitaev exchange couplings, respectively, and $\Gamma_{\alpha\beta}$ coefficients are the off-diagonal components of the symmetric anisotropic exchange matrix, with $\alpha, \beta = x, y, z$. A local Kitaev reference frame is used, such that for each Ir-Ir bond, the z -coordinate is perpendicular to the Ir_2O_2 plaquette.

TABLE I. Nearest neighbor magnetic couplings (in meV) for K_2IrO_3 and as obtained from spin-orbit MRCI calculations for the DFT-optimized structure. For comparison, the corresponding values for bonds $B1$ (top) and $B2$ (bottom) in Na_2IrO_3 are also mentioned (taken from Ref. [33]).

A_2IrO_3	$\angle\text{Ir-O-Ir}$	K	J	Γ_{xy}	$\Gamma_{yz} = -\Gamma_{zx}$
A = K	$95.0^\circ (\times 3)$	-6.3	1.3	5.2	-8.9
A = Na	$99.5^\circ (\times 1)$	-20.8	5.2	-0.7	-0.8
	$98.0^\circ (\times 2)$	-15.6	2.2	-1.1	0.8

The magnetic couplings were determined by mapping the *ab initio* data, obtained in the multi-reference configuration-interaction (MRCI) calculations including spin-orbit effects, onto the above effective spin Hamiltonian (Eq. (1)) following the scheme detailed in Ref. [12, 34, 35] and outlined later. Note that such a computational procedure has been successfully applied to other spin-orbit driven Mott insulators [12, 15, 21, 34–38].

The magnetic couplings thus obtained are listed in Table I. The most striking aspect is the unusually large off-diagonal exchange couplings, Γ -terms, approximately 10 times as compared to Na_2IrO_3 . This is accompanied by much smaller K and J . The ratio K/J , however, is comparable to the corresponding value in Na_2IrO_3 , implying that K_2IrO_3 is magnetically very frustrated. This further suggests that the magnetic anisotropy in K_2IrO_3 is large and dominated by the Γ -terms, unlike any other known spin-orbit-driven Mott insulator on a honeycomb lattice. Consequently, a fully anisotropic K - J - Γ Hamiltonian model would be necessary to describe this system. It is interesting to note that the magnetic couplings listed in Ref. [23] also suggest large off-diagonal couplings similar to our *ab initio* results. The mismatch in the magnitude of exchange couplings can be attributed to different methods employed, as also noticed in previous studies on honeycomb lattice Mott insulator α - RuCl_3 . [12, 39]

C. Role of C_3 symmetry and inter-layer species

In order to understand the origin of such large Γ 's, we study the (distinct) structural differences with Na_2IrO_3 . The characteristic features of the honeycomb planes in K_2IrO_3 are negligible trigonal distortions (due to large inter-layer separations) and a regular 120° arrangement of O-O links centered at Ir-Ir bonds when projected on the plane of Ir atoms (see Fig. 1(b)). Therefore, starting from K_2IrO_3 , an approximate lower symmetry structure similar to Na_2IrO_3 can be obtained in two steps: First, within the considered Ir_2O_{10} unit, the four outer O-O links are rotated about an axis perpendicular to the Ir plane and centered between the respective O-O links such that the structural unit retains the C_{2h} symmetry, albeit

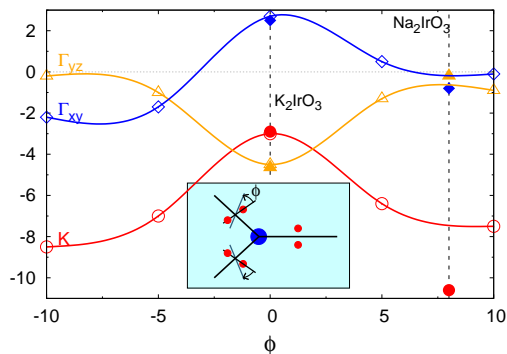


FIG. 2. Effects of C_3 point group symmetry on magnetic couplings: Magnetic exchange couplings (in meV) as a function of the relative twist angle ϕ of the O atoms away from the central Ir_2O_2 plaquette (open symbols). The inset shows the definition of ϕ , where Ir and the O atoms are represented by filled blue and red circles respectively. The vertical dashed lines represent the approximate ϕ values for K_2IrO_3 and bond $B1$ of Na_2IrO_3 , and the corresponding magnetic couplings are shown by filled symbols. The solid lines are guide to eye.

without the C_3 symmetry about the 'c' axis at the Ir sites. Due to the C_{2h} symmetry, these octahedral distortions can be quantified by a single parameter: twist angle ϕ which measures the deviation of the neighboring O-O links with respect to the O-O link in the central Ir_2O_2 plaquette (see the inset of Fig. 2). Second, introducing trigonal distortions with the trigonal axis perpendicular to Ir plane. We consider clusters with different values of ϕ and trigonal distortion. For consistency and comparison, same point charge embedding was used for all the cases (see Methods).

The dependence of the NN magnetic couplings on ϕ is shown in Fig. 2. The strength of the Kitaev exchange (Γ_{yz}) increases (decreases) away from the constrained case ($\phi = 0$) while Γ_{xy} changes sign. The NN Heisenberg exchange J , on the other hand, has a qualitatively similar behavior as K , and lies in the range of 2 meV and 3.7 meV (not shown). The corresponding values for the Ir_2O_{10} structural units of K_2IrO_3 and Na_2IrO_3 are also shown. The strength of the K and J parameters are substantially larger in the presence of trigonal distortion, as evidenced from the values for Na_2IrO_3 (filled symbols at $\phi \approx 8^\circ$ in Fig. 2) and also noted earlier [40]. We emphasize that the magnetic exchange couplings for the Ir_2O_{10} units in Fig. 2 are obtained within the MRCI framework, and thus provide a reliable qualitative estimate on their evolution with ϕ . However, a full chemical treatment of the NN octahedral units is required to obtain a good quantitative estimate of magnetic exchange interactions, as done for the values in Table 1 (see Methods for details).

Presence of smaller Na ion at the center of hexagons in the honeycomb layer in Na_2IrO_3 leads to deviations from the 120° order. The O atoms reorganize themselves

to lower the total energy. This is confirmed by comparing the total energy of Na_2IrO_3 and an equivalent structure derived from K_2IrO_3 such that the unit cell volume, and Ir-Ir and Ir-O distances for these two structures are comparable (see Methods). Na_2IrO_3 is found to be approximately 18 meV/atom lower in energy, thus establishing that the presence of larger intra-honeycomb-layer K ions leads to constraints in the relative orientation of the O atoms which, in turn, leads to large Γ 's. Similar nearly- 120° arrangement for the O-O links is also found in the hyper-honeycomb compound $\beta\text{-Li}_2\text{IrO}_6$ which also has somewhat larger Γ 's [19].

These results suggest that the real space C_3 symmetry at the Ir sites is intricately related to the strong magnetic anisotropy. Even small deviations significantly influence the magnetic couplings, suggesting strong entanglement between real space and spin space. As a result, the NN magnetic interactions are strongly frustrated, highly anisotropic in spin space and dominated by the Γ -terms. While a sizable Γ_{yz} in such a situation is plausible for large trigonal distortions [41], it is interesting that unusually large Γ_{ij} 's in K_2IrO_3 is realized even in the absence of sizable trigonal distortions.

It is important to note the fully anisotropic nature of the above J - K - Γ model. In comparison, some of the previously studied models consider only one component of Γ per bond [25–28]. On the other hand, in the fully anisotropic model for Na_2IrO_3 [33] and $\alpha\text{-RuCl}_3$ [12], the Γ terms turn out to be small. Nevertheless, they may have important consequences for magnetism [26–28]. In this regard, the implications of such large Γ 's, especially on the stability of a SL state, is particularly interesting.

D. Phase Diagram for the K - J - Γ model

We employ exact diagonalization (ED) calculations for the lattice realization of the fully anisotropic K - J - Γ model described by Eq. (1) on a 24-site cluster [5, 12, 15, 16]. The resulting magnetic phase diagram in the $\Gamma_{xy} - \Gamma_{yz}$ plane is very rich due to competing magnetic interactions, shown in Fig. 3(a) where the MRCI values of $J = 1.3$ and $K = -6.3$ were fixed. It includes six ordered phases: ferromagnetic (FM), Néel, zigzag, stripy, 3-fold spin-density wave (SDW), and incommensurate (IC) (see the Supplemental Material for details).

The most remarkable feature is that a (Γ -driven) SL state is found to be stable in a large region of the phase diagram although a stripy state is realized at small values of Γ_{ij} . It suggests an alternative route to realize a SL state in spin-orbit driven Mott insulators on a honeycomb lattice. Especially, it is striking that a Kitaev-type SL is recovered between the FM and stripy phases (see the Supplemental Material). The FM–Kitaev–SL–stripy path also appears when K/J is varied in the K - J model [5], implying that the ratio K/J could be effectively controlled by the Γ terms. The remaining SL region is

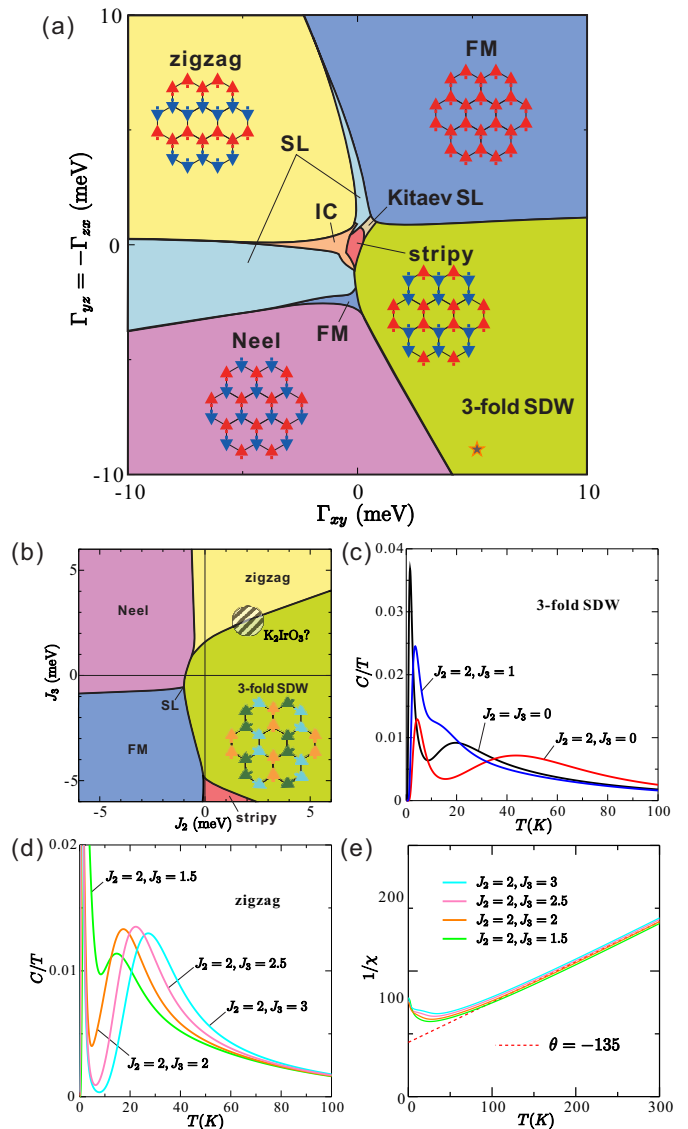


FIG. 3. Ground state phase diagram by ED with a 24-site cluster: (a) in the $\Gamma_{xy} - \Gamma_{yz}$ plane using the MRCI values of J and K ; (b) in the J_2 - J_3 plane using the MRCI values of J , K , Γ_{xy} , and Γ_{yz} . Schematic spin configurations are also shown. The star symbol in (a) indicates the position of MRCI parameter set and it corresponds to the origin in (b). A realistic range for K_2IrO_3 is located with shaded area in (b). Specific heat for the (c) 3-fold SDW and (d) zigzag phases, obtained by the ED calculations with a 12-site cluster. (e) Inverse magnetic susceptibility for the most likely realistic values of the extended range Heisenberg couplings J_2 and J_3 . The dotted line is $\chi = 2.1/(T - \theta)$ with $\theta = -135$ K.

is characterized as a frustration-induced “conventional” disordered state. A relatively wide region of SL phase exists for $\Gamma_{ij} < 0$; whereas, with increasing $\Gamma_{ij} > 0$, a SL state is stable only for small range, eventually leading to the FM order. This is consistent with an earlier work for the K - Γ model [26].

Let us now consider the situation for K_2IrO_3 . As

indicated in Fig. 3(a), the *pure* MRCI parameter set ($\Gamma_{xy} = 5.2$ meV, $\Gamma_{yz} = -8.9$ meV) stands on the 3-fold SDW ordered phase. However, extended range Heisenberg couplings J_2 and J_3 are known to be important for a honeycomb lattice spin-orbit driven Mott insulators [15]. Thus, we obtain a phase diagram considering J_2 and J_3 couplings in addition to the MRCI parameter set, which is shown in Fig. 3(b). To estimate realistic values of J_2 and J_3 for K_2IrO_3 , we turn towards the recent experimental observations.[24] Key features of the experimental specific heat are a broad maximum around 30K and finite C/T down to 1.8K. As shown in Fig. 3(c)(d), the broad peak at $\sim 30\text{K}$ can be numerically reproduced by setting $J_2 \sim 2$ and $J_3 \sim 2-3$. Given these values, the system is just near the boundary between the zigzag and 3-fold SDW phases (see Fig. 3(b)). Therefore, a strong competition between different orders is naturally expected, possibly explaining why no long-range order has been observed down to $\sim 2\text{K}$. Actually, the related Néel temperature is found to be $T_N < 2\text{K}$ in the numerical calculations of specific heat. The corresponding inverse magnetic susceptibility for the zigzag state in an external magnetic field of 2T perpendicular to the honeycomb planes leads to $\theta \sim -135\text{K}$ (Fig. 3(e)) which is somewhat smaller than the experimental value of $\theta \sim -180\text{K}$. [24] Nonetheless, the zigzag state is the most probable ground state.

The synthesized $\text{K}_x\text{Ir}_y\text{O}_2$ samples are non-stoichiometric and possess significant disorder in the form of vacancies in the K-layer and presence of Ir/K occupancy at the centers of the hexagons in the honeycomb layers. As was recently shown [21, 38], disorder, especially vacancies and position of the inter-layer cation, can significantly influence the magnetic couplings, and may possibly drive the system towards a SL state. However, a detailed study of such effects require considerations beyond the scope of the present work.

III. CONCLUSIONS

In summary, we have investigated the magnetic interactions and the possibility of QSL states in a structural model for honeycomb lattice Mott insulator featuring C_3 symmetry at the TM ion sites by considering the recently proposed structural model for K_2IrO_3 . We find that the resulting magnetic anisotropy is dominated by unusually large off-diagonal anisotropic exchange couplings. Such large Γ 's are related to the C_3 PG symmetry at the Ir sites, leading to constraints on the relative arrangement of O atoms. Despite small values of K and J as compared to Na_2IrO_3 , the sizable K/J ratio motivates a fully anisotropic K - J - Γ model for K_2IrO_3 leading to strong magnetic frustration. Large quantum fluctuations suppress the magnetic ordering down to $\sim 2\text{K}$.

A fully anisotropic K - J - Γ Hamiltonian with large Γ

terms is a generic feature of honeycomb Mott insulators with C_3 PG symmetry at the TM-ion sites and has a rich magnetic phase diagram. We highlight that the relative sign of Γ_{ij} is critical for the stability of a SL state. The most remarkable aspect is the hitherto unexplored possibility that a SL can be stabilized even for small values of $\Gamma < 0$ when K is ferromagnetic and the ratio $|K/J|$ is relatively large ($\gtrsim 5$). At the same time, the recognized FM–Kitaev–SL–stripy path of the K - J model is also recovered at finite Γ_{ij} . While the search for a SL state in spin-orbit driven Mott insulators so far is focused on tuning the ratio K/J , our findings suggest that tuning the off-diagonal anisotropic couplings in materials with $K < 0$ should also be promising.

IV. METHODS

A. Density Functional Calculations.

Density Functional Theory (DFT) calculations were performed using the Perdew-Burke-Ernzerhof (PBE) implementation of the generalized gradient approximation (GGA) as implemented in the FPLO code [42], version 18.52 [43]. A k -mesh with $12 \times 12 \times 12$ intervals in the full Brillouin zone was used for numerical integration along with a linear tetrahedron method. For the electronic properties, the ‘Atomic Limit’ (AL) implementation of the GGA+ U functional was used. The spin-orbit effects were considered within the 4-spinor formalism. For simplicity, the quantization axis was chosen to be $[0\ 0\ 1]$.

The structure optimization was performed for the internal parameters only, utilizing the space group $P6_322$ (# 182) and including the scalar relativistic corrections. The experimental values of the external parameters (lattice constants): $a = b = 5.282 \text{ \AA}$, $c = 13.544 \text{ \AA}$ [23] were used. The residual force is less than 1 meV/Å on each atom. The optimal atomic positions are presented in the Supplemental Material.

B. Quantum chemistry calculations.

To determine the strength of NN magnetic couplings for the DFT-optimized structure, quantum chemistry calculations were performed on a material model consisting of two NN edge shared octahedra unit Ir_2O_{10} . Additionally, the four octahedra sharing edge with the central unit along with eighteen NN K ions were also explicitly included in the calculations to account for the finite charge distribution in the immediate neighborhood. The remaining solid-state surroundings were modeled by arrays of point charges such that they reproduce the ionic Madelung potential in the cluster region. Energy-consistent relativistic pseudopotentials along with quadruple-zeta basis functions were used

for the Ir ions [44] of the central unit while an all-electron quintuple-zeta basis sets were employed for the bridging O ligands [45]. The remaining O atoms in the two-octahedra central region were described using an all-electron basis sets of triple-zeta quality [45]. Ir⁴⁺ sites belonging to the octahedra adjacent to the reference unit were described as closed-shell Pt⁴⁺ t_{2g}^6 ions, using relativistic pseudopotentials and valence triple-zeta basis functions [44]. Ligands belonging to these adjacent octahedra which are not shared with the central (reference) unit were modeled with a minimal all-electron atomic-natural-orbital basis sets [46]. All occupied shells of NN K⁺ sites were represented by using pseudopotentials and each of the K 4s orbitals were described with a single basis function [47]. All quantum chemistry computations were performed using the quantum chemistry package MOLPRO.

The magnetic couplings in Table I were obtained by mapping the *ab initio* data, obtained in the multi-reference configuration-interaction (MRCI) and including spin-orbit effects, as mentioned in the main text, onto an effective spin Hamiltonian (see Eq. (1) in the main text) following the scheme detailed in Ref. [12].

In the first step, complete-active-space self-consistent-field (CASSCF) calculations [2] were carried out for an average of the lowest nine singlet and nine triplet states, essentially of $t_{2g}^5 - t_{2g}^5$ character. Since CASSCF calculations also account for superexchange processes of $t_{2g}^6 - t_{2g}^4$ type in addition to NN $t_{2g}^5 - t_{2g}^5$ direct exchange, CASSCF wavefunctions also consist of a finite weight contribution from inter-site excitations of $t_{2g}^6 - t_{2g}^4$ type. Single and double excitations from the transition metal d (t_{2g}) and bridging-ligand p valence-shells were accounted for in the subsequent multireference configuration-interaction (MRCI) computations. The low-lying nine singlet and nine triplet states were considered in the spin-orbit treatment, in both CASSCF and MRCI calculations. In the next step, the *ab initio* quantum-chemistry data were mapped onto an effective spin Hamiltonian (Eq. (1) in the main text) which involves only the lowest four spin-orbit states, associated with the different possible couplings of the two NN 1/2 pseudospins. The other 32 spin-orbit levels arising from the $t_{2g}^5 - t_{2g}^5$ configuration involve $j_{\text{eff}} \approx 3/2$ to $j_{\text{eff}} \approx 1/2$ excitations and lie at significantly higher energy [15, 37]. The mapping was performed following the procedure described in Ref. [[12]]. The magnetic couplings shown in Table 1 in the main text are obtained by following this procedure.

C. Tests for the role of C_3 point group symmetry.

To further test our claim that C_3 point group symmetry at each Ir site is crucial to the strength of off-diagonal exchange couplings, we performed an additional set of quantum chemistry calculations using an edge shared octahedra unit $[\text{Ir}_2\text{O}_{10}]^{2-}$ as the central region.

We begin with a $[\text{Ir}_2\text{O}_{10}]^{2-}$ structural unit obtained from an idealized crystalline structure displaying C_3 point group symmetry about an axis perpendicular to the honeycomb plane (c' -axis) at each Ir site. The structural unit, therefore, has C_{2h} point group symmetry. All adjacent Ir and K sites were modeled as identical point charges to make the whole system charge neutral. Using this model, *ab initio* spin-orbit calculations at the MRCI level were carried out to obtain effective coupling parameters.

In the next step, we reduced the symmetry of the $[\text{Ir}_2\text{O}_{10}]^{2-}$ structural unit such that only C_{2h} symmetry of the cluster is retained while the C_3 point group symmetry at each Ir site is lost. This was obtained by keeping the central plaquette unchanged (i.e. no modifications to Ir-Ir or Ir-O bond lengths and Ir-O-Ir bond angles within this plaquette). However, the other sets of O atoms (representing the other two plaquette at each site) were rotated about an axis passing through the center of the O-O links and perpendicular to the hexagonal plane spanned by the Ir atoms. The positions of all such O atoms are connected by the two-fold rotation about the Ir-Ir axis and the mirror plane perpendicular to the Ir-Ir bond, which defines the C_{2h} symmetry. The resulting structures can therefore be characterized by a single “twist angle” ϕ (see Fig 2, main text). The structural positions of all the atoms for $\phi = 0$ and $\phi = 10^\circ$ is presented in Table S4. The magnetic couplings were then obtained for different structures corresponding to different values of ϕ by keeping the point charge embedding same as in the first step ($\phi = 0$).

The modification of the O sites corresponding to the NN plaquette affects the Ir d orbitals in a way that results in an increase in Kitaev exchange while decreasing the off-diagonal exchange components at the same time. MRCI spin-orbit results obtained for two site clusters with varying ϕ are shown in Fig. 2 in the main text. The model structure with $\phi = 0$ corresponds to the crystalline structure proposed for K_2IrO_3 while the model structure with $\phi = 10^\circ$ can be compared with the crystal structure of Na_2IrO_3 .

Basis sets of the same quality as discussed in the previous section were used for the structural unit in these calculations. Additionally, to access the reliability of these test calculations we performed checks by changing the embedding to the one with a lower symmetry arising due to the distortions. We find that the qualitative trend obtained in these calculations remains the same as shown in Fig. 2 in the main text.

D. Exact diagonalization calculations.

To investigate the lattice magnetic structure, we calculated the static spin-structure factor

$$S(\mathbf{Q}) = \frac{1}{N} \sum_{ij} \langle \tilde{\mathbf{S}}_i \cdot \tilde{\mathbf{S}}_j \rangle \exp[i\mathbf{Q} \cdot (\mathbf{r}_i - \mathbf{r}_j)], \quad (2)$$

where N is the number of sites in a periodic cluster and \mathbf{r}_i is the position of site i . The structure factors $S(\mathbf{Q})$ for representative momenta (first Brillouin zone) in different phases is shown in the Supplemental Material. Distinction between different states realized in the phase diagram (Fig. 3(a)), especially between the ordered and incommensurate phase, and between the ‘conventional’ (non-Kitaev-type) and Kitaev-type spin liquid (SL) states is illustrated. Further, the implication of finite cluster size is also discussed.

The phase boundaries were obtained by checking the second derivatives of the ground-state energy E_0/N and the total spin $2S_{\text{tot}}/N$ with respect to particular parameters. The critical Γ ’s values for the phase transitions were estimated from the peak positions in the second derivative of the ground-state energy $-\partial^2 E_0/\partial\Gamma_{yz}$ (see Supplemental Materials for a detailed discussion and illustration of the SL–IC–stripy–Kitaev SL–FM phase transitions).

To characterize the topological nature of the spin liquid

state, the hexagonal plaquette operator was considered, which is defined as [48]:

$$O_h = 2^6 \tilde{S}_1^x \tilde{S}_2^y \tilde{S}_3^z \tilde{S}_4^x \tilde{S}_5^y \tilde{S}_6^z, \quad (3)$$

where the site labels (subscripts) correspond to the six sites in a hexagonal ring and the link labels (superscripts) denote the corresponding bond anisotropy for bonds away from the hexagonal ring (see Supplemental Materials for details).

Acknowledgment. We thank Yogesh Singh for the structural data which motivated this study, and Liviu Hozoi for helpful discussions. Part of this work is supported by the DFG through SFB 1143 project A05. RR and MR acknowledge financial support from the European Union (ERDF) and the Free State of Saxony via the ESF project 100231947 and 100339533 (Young Investigators Group Computer Simulations for Materials Design - CoSiMa.) We also thank Ulrike Nitzsche for technical support.

-
- [1] A. Banerjee, C. Bridges, J.-Q. Yan, A. Aczel, L. Li, M. Stone, G. Granroth, M. Lumsden, Y. Yiu, J. Knolle, *et al.*, *Nature materials* **15**, 733 (2016).
- [2] T. Helgaker, P. Jørgensen, and J. Olsen, “*Molecular Electronic-Structure Theory*” (“Wiley, Chichester”, “2000”).
- [3] J. Kim, M. Daghofer, A. H. Said, T. Gog, J. van den Brink, G. Khaliullin, and B. J. Kim, *Nat. Commun.* **5**, 4453 (2014).
- [4] A. Lupascu, J. P. Clancy, H. Gretarsson, Z. Nie, J. Nichols, J. Terzic, G. Cao, S. S. A. Seo, Z. Islam, M. H. Upton, J. Kim, A. H. Said, D. Casa, T. Gog, V. M. Katukuri, H. Stoll, L. Hozoi, J. van den Brink, and Y.-J. Kim, “*Phys. Rev. Lett.*” ”**112**”, “147201” (“2014”).
- [5] J. Chaloupka, G. Jackeli, and G. Khaliullin, *Phys. Rev. Lett.* **105**, 027204 (2010).
- [6] S. K. Choi, R. Coldea, A. N. Kolmogorov, T. Lancaster, I. I. Mazin, S. J. Blundell, P. G. Radaelli, Y. Singh, P. Gegenwart, K. R. Choi, S.-W. Cheong, P. J. Baker, C. Stock, and J. Taylor, *Phys. Rev. Lett.* **108**, 127204 (2012).
- [7] S. H. Chun, J.-W. Kim, J. Kim, H. Zheng, C. C. Stoumpos, C. D. Malliakas, J. F. Mitchell, K. Mehlawat, Y. Singh, Y. Choi, T. Gog, A. Al-Zein, M. M. Sala, M. Krisch, J. Chaloupka, G. Jackeli, G. Khaliullin, and B. J. Kim, *Nat. Phys.* **11**, 462 (2015).
- [8] Y. Singh, S. Manni, J. Reuther, T. Berlijn, R. Thomale, W. Ku, S. Trebst, and P. Gegenwart, *Phys. Rev. Lett.* **108**, 127203 (2012).
- [9] I. I. Mazin, S. Manni, K. Foyevtsova, H. O. Jeschke, P. Gegenwart, and R. Valentí, *Phys. Rev. B* **88**, 035115 (2013).
- [10] K. W. Plumb, J. P. Clancy, L. J. Sandilands, V. V. Shankar, Y. F. Hu, K. S. Burch, H.-Y. Kee, and Y.-J. Kim, *Phys. Rev. B* **90**, 041112 (2014).
- [11] A. Banerjee, C. Bridges, J.-Q. Yan, A. Aczel, L. Li, M. Stone, G. Granroth, M. Lumsden, Y. Yiu, J. Knolle, *et al.*, *Nature Materials* **15**, 733 (2016).
- [12] R. Yadav, N. A. Bogdanov, V. M. Katukuri, S. Nishimoto, J. van den Brink, and L. Hozoi, *Sci. Rep.* **6**, 37925 (2016).
- [13] I. Kimchi and Y.-Z. You, *Phys. Rev. B* **84**, 180407 (2011).
- [14] J. G. Rau, E. K.-H. Lee, and H.-Y. Kee, *Phys. Rev. Lett.* **112**, 077204 (2014).
- [15] V. M. Katukuri, S. Nishimoto, V. Yushankhai, A. Stoyanova, H. Kandpal, S. Choi, R. Coldea, I. Rousochatzakis, L. Hozoi, and J. van den Brink, *New J. Phys.* **16**, 013056 (2014).
- [16] S. Nishimoto, V. M. Katukuri, V. Yushankhai, H. Stoll, U. K. Rößler, L. Hozoi, I. Rousochatzakis, and J. van den Brink, *Nat. Commun.* **7**, 10273 (2016).
- [17] A. Banerjee, P. Lampen-Kelley, J. Knolle, C. Balz, A. A. Aczel, B. Winn, Y. Liu, D. Pajerowski, J. Yan, C. A. Bridges, *et al.*, *npj Quantum Materials* **3**, 8 (2018).
- [18] G. Bastien, G. Garbarino, R. Yadav, F. J. Martinez-Casado, R. Beltrán Rodríguez, Q. Stahl, M. Kusch, S. P. Limandri, R. Ray, P. Lampen-Kelley, D. G. Mandrus, S. E. Nagler, M. Roslova, A. Isaeva, T. Doert, L. Hozoi, A. U. B. Wolter, B. Büchner, J. Geck, and J. van den Brink, *Phys. Rev. B* **97**, 241108 (2018).
- [19] M. Majumder, R. S. Manna, G. Simutis, J. C. Orain, T. Dey, F. Freund, A. Jesche, R. Khasanov, P. K. Biswas, E. Bykova, N. Dubrovinskaia, L. S. Dubrovinsky, R. Yadav, L. Hozoi, S. Nishimoto, A. A. Tsirlin, and P. Gegenwart, *Phys. Rev. Lett.* **120**, 237202 (2018).
- [20] G. Simutis, N. Barbero, K. Rolfs, P. Leroy-Calatayud, K. Mehlawat, R. Khasanov, H. Luetkens, E. Pomjakushina, Y. Singh, H.-R. Ott, J. Mesot, A. Amato, and T. Shiroka, *Phys. Rev. B* **98**, 104421 (2018).
- [21] R. Yadav, R. Ray, M. S. Eldeeb, S. Nishimoto, L. Hozoi, and J. van den Brink, *Phys. Rev. Lett.* **121**, 197203 (2018).
- [22] A. Koitzsch, C. Habenicht, E. Mueller, M. Knupfer, B. Büchner, S. Kretschmer, M. Richter, J. van den Brink, F. Boerrnert, D. Nowak, *et al.*, *Physical Review Materials*

- 1, 052001 (2017).
- [23] R. D. Johnson, I. Broeders, K. Mehlawat, Y. Li, Y. Singh, R. Valenti, and R. Coldea, (2019), arXiv:1908.04584.
 - [24] K. Mehlawat and Y. Singh, (2019), arXiv:1908.08475.
 - [25] I. Rousochatzakis and N. B. Perkins, *Physical review letters* **118**, 147204 (2017).
 - [26] A. Catuneanu, Y. Yamaji, G. Wachtel, Y. B. Kim, and H.-Y. Kee, *npj Quantum Materials* **3**, 23 (2018).
 - [27] P. Lampen-Kelley, S. Rachel, J. Reuther, J.-Q. Yan, A. Banerjee, C. A. Bridges, H. B. Cao, S. E. Nagler, and D. Mandrus, *Phys. Rev. B* **98**, 100403 (2018).
 - [28] M. Gohlke, G. Wachtel, Y. Yamaji, F. Pollmann, and Y. B. Kim, *Phys. Rev. B* **97**, 075126 (2018).
 - [29] H. Gretarsson, J. P. Clancy, X. Liu, J. P. Hill, E. Bozin, Y. Singh, S. Manni, P. Gegenwart, J. Kim, A. H. Said, D. Casa, T. Gog, M. H. Upton, H.-S. Kim, J. Yu, V. M. Katukuri, L. Hozoi, J. van den Brink, and Y.-J. Kim, *Phys. Rev. Lett.* **110**, 076402 (2013).
 - [30] G. Jackeli and G. Khaliullin, *Phys. Rev. Lett.* **102**, 017205 (2009).
 - [31] A. Abragam and B. Bleaney, *Electron Paramagnetic Resonance of Transition Ions* (Clarendon Press, 1970).
 - [32] B. J. Kim, H. Jin, S. J. Moon, J.-Y. Kim, B.-G. Park, C. S. Leem, J. Yu, T. W. Noh, C. Kim, S.-J. Oh, J.-H. Park, V. Durairaj, G. Cao, and E. Rotenberg, *Phys. Rev. Lett.* **101**, 076402 (2008).
 - [33] R. Yadav, S. Rachel, L. Hozoi, J. van den Brink, and G. Jackeli, *Physical Review B* **98**, 121107 (2018).
 - [34] N. A. Bogdanov, V. M. Katukuri, J. Romhányi, V. Yushankhai, V. Kataev, B. Büchner, J. van den Brink, and L. Hozoi, *Nat. Commun.* **6**, 7306 (2015).
 - [35] R. Yadav, M. Pereiro, N. A. Bogdanov, S. Nishimoto, A. Bergman, O. Eriksson, J. van den Brink, and L. Hozoi, *Phys. Rev. Materials* **2**, 074408 (2018).
 - [36] N. A. Bogdanov, V. M. Katukuri, H. Stoll, J. van den Brink, and L. Hozoi, *Phys. Rev. B* **85**, 235147 (2012).
 - [37] V. M. Katukuri, R. Yadav, L. Hozoi, S. Nishimoto, and J. van den Brink, *Sci. Rep.* **6**, 29585 (2016).
 - [38] R. Yadav, M. S. Eldeeb, R. Ray, S. Aswartham, M. I. Sturza, S. Nishimoto, J. van den Brink, and L. Hozoi, *Chemical science* **10**, 1866 (2019).
 - [39] S. M. Winter, Y. Li, H. O. Jeschke, and R. Valentí, *Phys. Rev. B* **93**, 214431 (2016).
 - [40] S. Nishimoto, V. M. Katukuri, V. Yushankhai, H. Stoll, U. K. Rößler, L. Hozoi, I. Rousochatzakis, and J. Van Den Brink, *Nature communications* **7**, 10273 (2016).
 - [41] J. Chaloupka and G. Khaliullin, *Physical Review B* **92**, 024413 (2015).
 - [42] K. Koepnik and H. Eschrig, *Phys. Rev. B* **59**, 1743 (1999).
 - [43] <https://www.fplo.de>.
 - [44] D. Figgen, K. A. Peterson, M. Dolg, and H. Stoll, *J. Chem. Phys.* **130**, 164108 (2009).
 - [45] T. H. Dunning, *J. Chem. Phys.* **90**, 1007 (1989).
 - [46] K. Pierloot, B. Dumez, P.-O. Widmark, and B. O. Roos, *Theor. Chim. Acta* **90**, 87 (1995).
 - [47] P. Fuentealba, H. Preuss, H. Stoll, and L. V. Szentpaly, *Chemical Physics Letters* **89**, 418 (1982).
 - [48] A. Kitaev, *Ann. Phys.* **321**, 2 (2006).

SUPPLEMENTAL MATERIAL

I. STRUCTURAL DETAILS AND ELECTRONIC PROPERTIES

A. Optimized structure

The optimal atomic positions for K_2IrO_3 are listed in Table S1, and are in good agreement with the reported values [23]. Note that the nearest neighbor octahedra are of slightly different sizes as implied by different Ir-O bond lengths. Therefore, at each Ir-Ir bond, inversion and mirror symmetry are absent. Consequently, the Ir_2O_{10} clusters do not have C_{2h} symmetry. However, deviation from the C_{2h} symmetry is only marginal as the Ir-O bond lengths differ by $\lesssim 0.19\%$. Therefore, C_{2h} symmetry is a reasonable approximation and is used in the quantum chemistry calculations.

TABLE S1. Optimal atomic positions and related structural parameters in K_2IrO_3 . The external parameters are kept fixed to the experimental value [23]: space group $P6_322$ (# 182) with $a = b = 5.282 \text{ \AA}$, $c = 13.544 \text{ \AA}$.

Atom.	Wyk-pos	Coordinates ($x/a, y/b, z/c$)
Ir1	2b	(0, 0, 1/4)
Ir2	2c	(1/3, 2/3, 1/4)
K1	2c	(2/3, 1/3, 1/4)
K2	6g	(0.3404, 0.3404, 1/2)
O	2a	(0.3328, 0.0593, -0.3442)
Param.	Values	
$d_{\text{Ir-Ir}}$ (Å)	3.0496	
$d_{\text{Ir-O}}$ (Å)	2.065, 2.069	
$d_{\text{Ir-layers}}$ (Å)	6.77	
$\angle \text{Ir-Ir-Ir}$	120°	
$\angle \text{Ir-O-Ir}$	95.06°	

B. Electronic Properties

Figure S1 shows the total and partial density of states (DOS) for K_2IrO_3 with $U = 1.2 \text{ eV}$ and $J = 0.3 \text{ eV}$ applied to the Ir-5d states. For comparison, the total DOS for Na_2IrO_3 with the reported lattice parameters [6] and optimized internal parameters, and with the same U and J values for the Ir-5d states is also shown. The $d-t_{2g}$ and $d-e_g$ states are also marked. The clear splitting of the $d-t_{2g}$ bands into $j_{\text{eff}} = 3/2$ and $1/2$ states is evident, implying that K_2IrO_3 is a spin-orbit driven Mott insulator. The ground state properties, especially the magnetic moments and residual charges, are comparable with Na_2IrO_3 , as shown in Table S2.

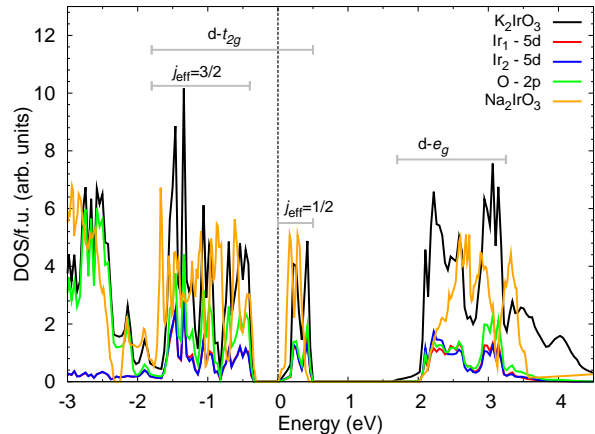


FIG. S1. Total (spin-up + spin-down) density of states (DOS) per formula unit (f.u.) for the spin-orbit driven Mott Insulator K_2IrO_3 along with the contributions of Ir-5d and O-2p states as obtained within the GGA+ U scheme and considering spin-orbit effects, with $U_{\text{Ir-5d}} = 1.2 \text{ eV}$ and $J_{\text{Ir-5d}} = 0.3 \text{ eV}$. For comparison, the total DOS for Na_2IrO_3 with the same U and J values is also shown. The Fermi energy is shown by dashed vertical line.

C. Comparison with an equivalent Na_2IrO_3 structure — role of K-ions

To ascertain the relation between the C_3 point group symmetry at the Ir sites and the presence of the K ions at the center of the hexagons in the honeycomb layer, we performed DFT calculations with the following assertion: if the C_3 point group symmetry is a direct consequence of the larger K^+ ions, presence of smaller non-magnetic cation, such as Na^+ , would allow the O atoms to reorganize themselves to a lower symmetry structure and, subsequently, lower the total energy. Indeed, Na_2IrO_3 crystallizes in the space group $C2/m$ [6], which does not have the relative 120° arrangement of the O-O links (shown in Fig. 1(b) in the main text).

The truthfulness of this assertion was checked by comparing the ground state energies (within GGA) of the known structure of Na_2IrO_3 [6], but with optimized atomic positions, with an equivalent structure derived

TABLE S2. Comparison of the ground state magnetic properties of K_2IrO_3 and Na_2IrO_3 obtained within the GGA+ U scheme with spin-orbit coupling. $U = 1.2 \text{ eV}$ and $J = 0.3 \text{ eV}$ was applied to the Ir-5d states.

Param.	K_2IrO_3	Na_2IrO_3
$m_{\text{S}}^{\text{Ir}} (\mu_{\text{B}})$	0.574, 0.569	0.431
$m_{\text{S}}^{\text{O}} (\mu_{\text{B}})$	0.095	0.062, 0.061
$m_{\text{S}}^{\text{K/Na}} (\mu_{\text{B}})$	0.005, 0.002	0.003, 0.001
$m_{\text{S}}^{\text{tot}}$ (per f.u., $\mu_{\text{B}})$	0.864	0.620
$m_{\text{L}}^{\text{Ir}} (\mu_{\text{B}})$	0.862, 0.855	0.584

from K_2IrO_3 with the C_3 point group symmetry at the Ir sites, labeled as $\text{Na}_2\text{IrO}_3^*$. The equivalency between the two structures correspond to comparable Ir-Ir and Ir-O distances and the unit cell volume. $\text{Na}_2\text{IrO}_3^*$ was obtained from K_2IrO_3 in the following steps:

1. Replace all K ions by Na ions.
2. Tune a (and b) such that the Ir-Ir distances are comparable to that of Na_2IrO_3 .
3. Reduce c such that the unit cell volumes match while the inter-layer separations and the Ir-O distances are comparable to Na_2IrO_3 .
4. Optimize the atomic positions of the resulting structure.

The atomic positions and structural details of both the structures are presented in Table S3.

D. Structures away from C_3 point group symmetry

In order to test the effects of C_3 point group symmetry on the magnetic couplings, quantum chemical calculations were carried for $[\text{Ir}_2\text{O}_{10}]^{2-}$ structural units with different values of the twist angle, ϕ (see Methods for details). Away from $\phi = 0$, the structural units possess C_{2h} but not the C_3 point group symmetry. Table S4 lists the atomic positions for the $[\text{Ir}_2\text{O}_{10}]^{2-}$ structural units at $\phi = 0$ and $\phi = 10^\circ$. The corresponding values of the magnetic couplings were shown in Fig. 2.

TABLE S3. Comparison of the structural parameters between $\text{Na}_2\text{IrO}_3^*$ and Na_2IrO_3 . ‘*’ denotes that this structure was obtained from K_2IrO_3 such that the Ir-Ir distances and the unit cell volume are comparable with Na_2IrO_3 .

Atom.	$\text{Na}_2\text{IrO}_3^*$	Na_2IrO_3
Ir1	(0, 0, 1/4)	(0, -0.3338, 0)
Ir2	(1/3, 2/3, 1/4)	-
Na1	(2/3, 1/3, 1/4)	(0, 0, 0)
Na2	(0.3414, 0.3414, 1/2)	(0, -0.1598, 1/2)
Na3	-	(0.3404, 0.3404, 1/2)
O	(0.3332, 0.0291, 0.6449)	(-0.25284, 0.18314, -0.21001)
Param.		
Space Group	$P6_322$ (# 182)	$C2/m$ (# 12)
Volume/f.u. (\AA^3)	67.646	67.646
Energy difference/f.u. (meV)	107.89	0.0
$d_{\text{Ir-Ir}}$ (\AA)	3.12	3.12, 3.14
$d_{\text{Ir-O}}$ (\AA)	2.061, 2.0623	2.054, 2.061
$d_{\text{Ir-layers}}$ (\AA)	5.338	5.614
$\angle \text{Ir-Ir-Ir}$	120°	$120.12^\circ, 119.76^\circ$
$\angle \text{Ir-O-Ir}$	98.48°	99.344°

TABLE S4. Atomic positions of the atoms in the Ir_2O_{10} clusters for different values of the twist angle ϕ .

Atom.	x (\AA)	y (\AA)	z (\AA)
$\phi = 0$			
Ir1	0.000000	0.000000	0.000000
Ir2	3.049560	0.000000	0.000000
O1	1.524780	0.759692	1.170942
O2	1.524780	-0.759692	-1.170942
O3	-1.420303	0.940652	1.170942
O4	-0.104478	1.700344	-1.170942
O5	-0.104477	-1.700344	1.170942
O6	-1.420303	-0.940652	-1.170942
O7	4.469863	0.940652	1.170942
O8	3.154038	1.700344	-1.170942
O9	3.154037	-1.700345	1.170942
O10	4.469863	-0.940652	-1.170942
$\phi = 10^\circ$			
Ir1	0.000000	0.000000	0.000000
Ir2	3.049560	0.000000	0.000000
O1	1.524780	0.759692	1.170942
O2	1.524780	-0.759692	-1.170942
O3	-1.476267	1.060668	1.170942
O4	-0.048513	1.580328	-1.170942
O5	-0.048513	-1.580328	1.170942
O6	-1.476267	-1.060668	-1.170942
O7	4.525827	1.060668	1.170942
O8	3.098073	1.580328	-1.170942
O9	3.098073	-1.580328	1.170942
O10	4.525827	-1.060668	-1.170942

II. EXACT DIAGONALIZATION CALCULATIONS

A. Static spin-structure factor

The static spin-structure factor is defined as:

$$S(\mathbf{Q}) = \frac{1}{N} \sum_{ij} \langle \tilde{\mathbf{S}}_i \cdot \tilde{\mathbf{S}}_j \rangle \exp[i\mathbf{Q} \cdot (\mathbf{r}_i - \mathbf{r}_j)], \quad (1)$$

where N is the number of sites in a periodic cluster and \mathbf{r}_i is the position of site i . In Fig. S2 we show the structure factors $S(\mathbf{Q})$ for representative momenta (first Brillouin zone) in different phases. Typical Γ_{xy} and Γ_{yz} values were chosen for each phase. For the ordered phases the magnetic structure can be determined from the reciprocal-space Bragg-peak positions. In the incommensurate (IC) phase the Bragg-peak positions are shifted with varying Γ_{xy} and Γ_{yz} if the system is large enough. However, our system size is 24 and only discrete momenta are allowed. In such the case, usually, the dominant IC Bragg-peak position is moved from a IC momentum to another by transferring the weight with varying Γ_{xy} and Γ_{yz} . Also, it is worth noting the difference between the structure factors of the ‘conventional’ (non-Kitaev-type) and Kitaev-type spin liquid (SL) states. In the ‘conventional’ SL phase $S(\mathbf{Q})$ is structureless and the weight is widely distributed over

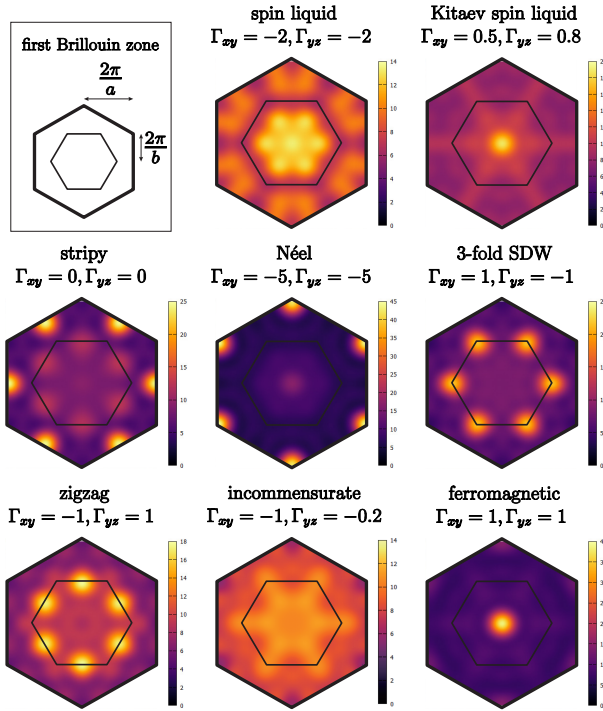


FIG. S2. Spin-structure factor $S(\mathbf{Q})$ for representative momenta in different phases.

the reciprocal space, reflecting a disordered spin state. Whereas, in the Kitaev-type SL phase the weight is very small for the whole \mathbf{Q} range because the spin-spin correlations except for the nearest-neighbor bond are very small. A peak at $\mathbf{Q} = \mathbf{0}$ is due to the finite-size effect. Further discussion about the spin-spin correlations is given below.

B. Quantum phase transition

To find the phase boundaries, we checked the second derivatives of the ground-state energy E_0/N and the total spin $2S_{\text{tot}}/N$ with respect to particular parameters. In Fig. S3(b) we illustrate four phase transitions (SL–IC–stripy–Kitaev SL–FM) with varying Γ_{xy} and Γ_{yz} along dashed line in Fig. S3(a). The critical Γ 's values were estimated from the peak positions in the second derivative of the ground-state energy $-\partial^2 E_0/\partial\Gamma_{yz}$; the SL–IC–stripy–Kitaev SL–FM phase transitions occur at $(\Gamma_{xy}, \Gamma_{yz}) = (-0.74875, -0.57)$, $(-0.54750, -0.34)$, $(0.25750, 0.58)$, and $(0.71250, 1.10)$, respectively. The former two transitions are of the first order, and the latter two are of the second order or continuous. Furthermore, we considered the hexagonal plaquette operator to check the topological property of the spin liquid state. The plaquette operator is an indicative quantity for the Kitaev-type spin liquid. It

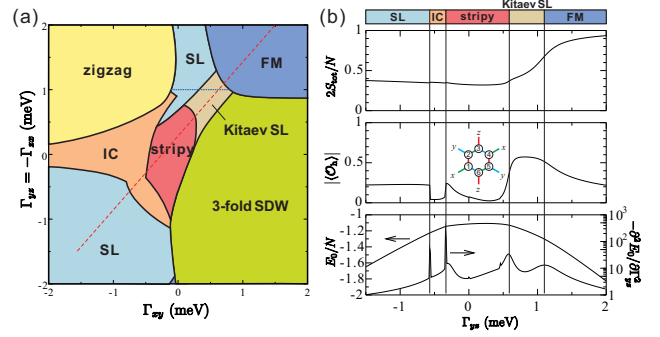


FIG. S3. (a) Ground-state phase diagram around $\Gamma_{xy} = \Gamma_{yz} = 0$, extracted from Fig. 3 in the main text. (b) Representative physical quantities for the 24-site periodic cluster as a function of Γ_{yz} along red dashed line ($\Gamma_{yz} = \frac{8}{7}\Gamma_{xy} + \frac{2}{7}$) in (a). Top: Total spin, Middle: Expectation value of the hexagonal plaquette operator, Bottom: Ground-state energy per site E_0/N and its second derivative $-\partial^2 E_0/\partial\Gamma_{yz}^2$.

is defined as [48]:

$$O_h = 2^6 \tilde{S}_1^x \tilde{S}_2^y \tilde{S}_3^z \tilde{S}_4^x \tilde{S}_5^y \tilde{S}_6^z, \quad (2)$$

where the labeling of links and sites is denoted in the middle panel of Fig. S3(b). In the pure Kitaev limit ($K \gg J, \Gamma$) the operator (Eq. 2) commutes with the Hamiltonian and the expectation value of $\langle O_h \rangle$ is exactly ± 1 . It is also known that it goes rapidly down to $\langle O_h \rangle \sim 0$ away from the Kitaev spin liquid regions [12]. As shown in Fig. S3(b), the plaquette operator is significantly enhanced in a spin liquid region at $0.25750 < \Gamma_{xy} < 0.71250$, $0.58 < \Gamma_{yz} < 1.10$. Thus, we conclude that this spin liquid is of the Kitaev-type. This is also consistent with almost weightless $S(\mathbf{Q})$ shown above.

C. Difference between Kitaev and non-Kitaev spin liquids

Sometimes, it is not easy to distinguish between Kitaev and non-Kitaev SL states because the phase transition is rather crossover-like. Nevertheless, they may be identified by looking at their spin-spin correlations (spin structure factor) and expectation value of the plaquette operator $\langle O_h \rangle$.

In general, the Kitaev SL state is characterized by a rapid decay of the spin-spin correlations: in the Kitaev limit, only the NN correlations are finite and longer-range ones are zero; accordingly, as shown in Fig. S2, the static spin structure factor has a single $\mathbf{Q} = \mathbf{0}$ peak, the weight of which is much smaller than that for a FM state, in a finite-size cluster. On the other hand, the spin-spin correlations for a non-Kitaev SL are also not long ranged but the decay length are typically much larger, i.e., like a power-law decay, than that for the Kitaev SL; thus, a structureless $S(\mathbf{Q})$ is obtained. This can be simply confirmed by considering the spin-spin correlations in

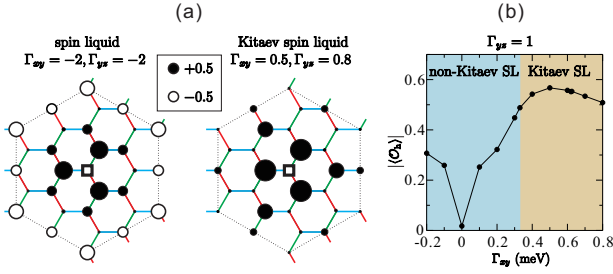


FIG. S4. Spin-spin correlation function $\langle \tilde{\mathbf{S}}_i \cdot \tilde{\mathbf{S}}_j \rangle$ for non-Kitaev and Kitaev SL states in our phase diagram [Fig. S3(a)]. The reference site i is denoted by open square and the value of $\langle \tilde{\mathbf{S}}_i \cdot \tilde{\mathbf{S}}_j \rangle$ at site j is expressed by a circle. The filled and open circles mean positive and negative values of $\langle \tilde{\mathbf{S}}_i \cdot \tilde{\mathbf{S}}_j \rangle$, respectively. The diameter of each circle is proportional to the magnitude, i.e., $|\langle \tilde{\mathbf{S}}_i \cdot \tilde{\mathbf{S}}_j \rangle|$. (b) Expectation value of the hexagonal plaquette operator $|\langle O_h \rangle|$ as a function of Γ_{xy} at $\Gamma_{yz} = 1$ fixed (along blue dotted line in Fig. S3(a)).

the real space. In Fig. S4(a) the real-space spin-spin correlations for non-Kitaev and Kitaev SL states are compared. We can obviously see that the correlation for Kitaev SL decays very rapidly and it is very small for longer distances than one lattice spacing; that for non-Kitaev SL decays much more slowly with distance.

We also show expectation value of the hexagonal plaquette operator $|\langle O_h \rangle|$ around the phase boundary between non-Kitaev and Kitaev SL phases in Fig. S4(b). A steep increase of $|\langle O_h \rangle|$ from non-Kitaev towards Kitaev SL phases is clearly seen.

D. Spin structure of the 3-fold SDW state

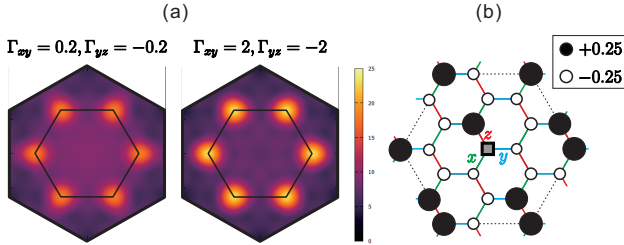


FIG. S5. (a) Spin-structure factor $S(\mathbf{Q})$ for $\Gamma_{xy} = 0.2$, $\Gamma_{yz} = -0.2$ and $\Gamma_{xy} = 2$, $\Gamma_{yz} = -2$, where the system is in the 3-fold SDW state. (b) Real-space spin-spin correlation function $\langle \tilde{\mathbf{S}}_i \cdot \tilde{\mathbf{S}}_j \rangle$ for a 3-fold SDW state ($\Gamma_{xy} = 5$, $\Gamma_{yz} = -5$). The reference site i is denoted by open square and the value of $\langle \tilde{\mathbf{S}}_i \cdot \tilde{\mathbf{S}}_j \rangle$ at site j is expressed by a circle. The filled and open circles mean positive and negative values of $\langle \tilde{\mathbf{S}}_i \cdot \tilde{\mathbf{S}}_j \rangle$, respectively. The diameter of each circle is proportional to the magnitude, i.e., $|\langle \tilde{\mathbf{S}}_i \cdot \tilde{\mathbf{S}}_j \rangle|$. To detect the symmetry-broken state, the reference site is pinned by an infinite local magnetic field.

As shown in our phase diagram [Fig. 3(a) in the main text], the ground state for a wide range of $\Gamma_{xy} >$ and

$\Gamma_{yz} <$ is characterized as a 3-fold SDW phase. The spin-structure factor $S(\mathbf{Q})$ for $\Gamma_{xy} = 0.2$, $\Gamma_{yz} = -0.2$ and $\Gamma_{xy} = 2$, $\Gamma_{yz} = -2$ are shown in Fig. S5(a). The set $\Gamma_{xy} = 0.2$, $\Gamma_{yz} = -0.2$ belongs to the 3-fold SDW ground state but is in the vicinity to neighboring stripy phase. Therefore, the peak structure in $S(\mathbf{Q})$ is still somewhat blurred. Roughly speaking, this phase is more stabilized as $\Gamma_{xy} \approx -\Gamma_{yz}$ increases. We have also confirmed that the 3-fold SDW state is maintained up to the limit of $\Gamma_{xy} \approx -\Gamma_{yz} = \infty$.

In order to see the spin structure of 3-fold SDW state, we calculate the real-space spin-spin correlation function $\langle \tilde{\mathbf{S}}_i \cdot \tilde{\mathbf{S}}_j \rangle$. The result is plotted in Fig. S5(b). A pinning is achieved by applying an infinite-strength magnetic field along z -axis on a site (referred as a reference site in Fig. S5(b)) to directly detect a symmetry-broken state with a periodic cluster. We can clearly see a SDW structure with 3-fold oscillation perpendicular to the z -bond.